European Rotorcraft Forum

TIP VORTEX STUDY OF A ROTOR WITH DOUBLE-SWEPT BLADE TIPS

C. Christian Wolf Johannes N. Braukmann
Institute of Aerodynamics and Flow Technology, German Aerospace Center (Germany)

Martin M. Müller
Institute of Aeroelasticity, German Aerospace Center (Germany)

Abstract
An experimental aerodynamic study was conducted, analyzing the wake structure of a four-bladed model rotor with a forward-backward swept tip geometry inspired by the ONERA-DLR "ERATO" design. Similar tip designs are used on some modern helicopter main rotors. The experiments were conducted at the rotor test stand Göttingen in hover-like conditions using a stereoscopic high-speed particle image velocimetry system. The results are compared with a reference rotor using a conventional parabolic blade tip. The test parameters include both constant-pitch cases and pitch-oscillating cases with a cyclic swashplate input. The constant-pitch tests show a two-step stall behavior for the double-swept tip, with the first step characterized by a reduced thrust slope and a reduced rotor efficiency. This effect is explained by a repositioning and a structural change of the tip vortex generation. The pitch-oscillating cases show that the double-swept tip results in an earlier tip stall compared to the parabolic geometry while maintaining high thrust levels. The dynamic tip stall yields a break-down of the wake's tip vortex system, which is replaced by a spanwise band with small-scale turbulent structures and trailed vorticity, but no large-scale vortices.

Nomenclature

A	Rotor plane area, $A = 1.33\,\mathrm{m}^2$
c	Chord length, $c = 0.072\,\mathrm{m}$
C_p	Pressure coefficient
C_T	Thrust coeff., $C_T = T/(\rho\pi R^2 V_{tip}^2)$
f	Rotor frequency, 1/s
M	Mach number
r	Radial coordinate in a tip vortex, m
R	Rotor radius, $R = 0.65\,\mathrm{m}$
Re	Reynolds number
t	Time, s
T	Rotor thrust, N
u, v, w	Cartesian velocity components, m/s
V_i	Induced velocity, m/s
V_{tip}	Blade tip velocity, m/s
V_θ	Tangential (swirl) velocity, m/s
x, y, z	Cartesian coordinate system, m

Greek symbols

Γ	Circulation, m^2/s
Γ_V	Vortex circulation at $r = 0.5c$, m^2/s
Θ	Root pitch angle, deg
ρ	Air density, $\mathrm{kg/m}^3$
λ_2	"Lambda-2" vortex criterion, 1/s
σ	Rotor solidity, $\sigma = 0.141$
Ψ	Azimuth angle, deg
Ψ_V	Tip vortex wake age, deg
ω	Out-of-plane vorticity, 1/s

Abbreviations and other symbols

BERP	British Experimental Rotor Programme
CFD	Computational fluid dynamics
DEHS	Di-ethyl-hexyl-sebacate
DLR	German Aerospace Center
DST	Double-swept blade tip
ERATO	Etude d'un Rotor Aéroacoustique Techologiquement Optimisé (aeroacoustically optimized rotor)
ONERA	Office national d'études et de recherches aérospatiales
PBT	Parabolic blade tip
PIV	Particle image velocimetry
PSP	Pressure-sensitive paint
RTG	Rotor test stand Göttingen
↑	Upstroke
↓	Downstroke

1. INTRODUCTION

Innovative blade tip designs with non-rectangular planforms have the potential to optimize the vibration, noise, and performance characteristics of helicopter rotors. A well-known example is the British Experimental Rotor Programme (BERP), with a "paddle tip"-design improving the blade aerodynamics in high-speed flight by increasing the surface area in the blade tip region. The swept-back outer leading edge not only reduces the effective Mach number and, thus, the drag on the advancing side, but also influences the tip vortex generation at high angles of attack on the retreating side. The latter effect is an intentional design feature "similar to a slender delta wing"[19], and has been optimized for a reduced vortex drag in the current "BERP IV"-generation[8]. The validity of the BERP design philosophy was demonstrated by comparison with other main rotor designs, for example the Apache rotor[38].

The ONERA-DLR "ERATO" design uses a double-swept tip shape[32] to reduce parallel blade-vortex interactions for improved rotor acoustics in forward flight conditions, with a reduced high-speed drag due to leading edge sweep as a byproduct. The initial ERATO shape was optimized iteratively[35], for example to avoid tip stall, and paved the way for the Airbus Blue Edge™-design and the Airbus H160 production rotor, see Fig. 1.

Figure 1: Fore-aft swept blade tip and tail section of the H160 helicopter[18].

Recent DLR studies on ERATO-inspired subscale blade models revisited the idea of tip planforms with fore-aft sweep, focusing on additional details such as the design of the tip shape and structure[16], aeroelastic aspects[13,15], and the dynamic stall-behavior[10,17,36].

The tip vortex also impacts the hover performance[37] in addition to the influence on the rotor's forward flight characteristics. For example, a comparison of different CFD codes by Wilke et al.[39] showed that the predicted aging or decay of the tip vortex structure affects the inflow of successive blades passing the same region. The resulting differences in separated flow regions over the blade tip is one of the primary sources for uncertainties in the predicted hover performance. The vortex aging in the rotor's near field can be described as a growth of the viscous core at almost constant circulation[1]. A correct quantification of the vortex parameters is still challenging for both numerical work, due to grid resolution or dissipation[5,9], and experimental work, due to measurement uncertainties to be discussed in the remainder of this paper.

The current work studies an experiment on the tip vortex system of a double-swept tip design applied to a four-bladed model rotor in hover-like conditions. The results cover both constant-pitch and pitch-oscillating test cases, and were acquired with high-speed particle image velocimetry (PIV) covering the wake flow up to an age corresponding to about one rotor revolution. The data was compared with a reference rotor with a rectangular planform and a conventional parabolic tip shape as investigated in earlier campaigns[2,41]. Additional blade design parameters, such as airfoil geometry, twist distribution, or anhedral tip designs[33] are not considered in the current study. In addition to the aerodynamic analysis, a particular focus was on parameters influencing the measurement uncertainty of the setup.

2. EXPERIMENTAL SETUP

2.1. Rotor blade geometry

Figure 2 (top) shows the rotor blade with double-swept tip (DST) as developed by Müller et al.[16], based on a pitching wing model by Lütke et al.[15]. The geometry comprises a blend of the EDI-M112 and EDI-M109 airfoils. The aerodynamic surface starts at $y/R = 0.25$, and the forward- and backward-swept segments start at about $y/R = 0.63$ and $y/R = 0.76$, respectively. Further outboard, the straight leading edge blends into a parabolic arc. The conventional reference design, see Schwermer et al.[28] and Fig. 2 (bottom), uses the DSA-9A airfoil geometry and has a rectangular planform with a parabolic blade tip (PBT) as seen on many current helicopter designs.

Both blades have a radius of $R = 650\,\mathrm{mm}$, a chord length of $c = 72\,\mathrm{mm}$, and a similar negative twist distribution summing up to about $-9°$ over the span, see Kaufmann et al.[10] for additional details. The rotational frequency of the rotors was set to $f = 24.0$ Hz (DST) and $f = 23.6$ Hz (PBT), resulting in Mach and chord-based Reynolds numbers of approximately $M = 0.21$ and $Re = 3.6 \cdot 10^5$ at 75% of

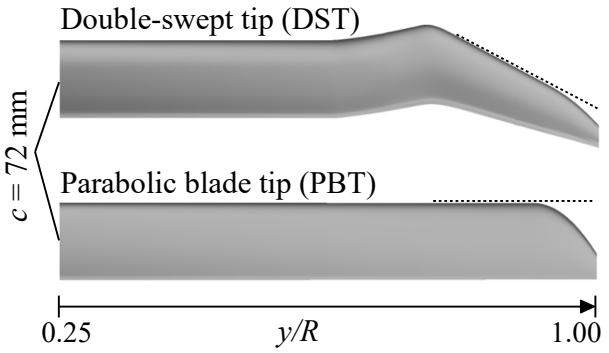

Figure 2: Blade planforms with double-swept tip (DST, top) and parabolic blade tip (PBT, bottom).

the tip radius. Both blades are made from carbon-fiber reinforced plastics.

2.2. Rotor test stand Göttingen (RTG)

The rotor test facility Göttingen (RTG)[27], see Fig. 3 (left), drives a horizontal rotor shaft and is equipped with a swashplate to adjust both the collective and cyclic pitch settings of the four-bladed rotors. In comparison to earlier publications, the swashplate actuation was upgraded with electronic stepper motors for a faster and more precise adjustment.

An Eiffel-type wind tunnel provides a slow axial inflow of $V_\infty \approx 2.2\,\mathrm{m/s}$ simulating climb conditions with a nondimensional rate of $V_\infty/V_{tip} = 0.022$. The inflow is used to prevent recirculation within the test chamber[3] and to convect the rotor wake in the downstream direction and through exit doors. The test chamber is large in comparison to the rotor radius, R, with dimensions of $20.6\,R \times 13.2\,R \times 11.0\,R$ (length×width×height). The standard measurement systems of the RTG feature rotor thrust and torque sensors, an azimuth encoder, and a telemetry system for blade-mounted pitch sensors, strain gauges, and fast-response surface pressure transducers. Data is stored at $50\,\mathrm{kHz}$ by a digital recorder, which is also used to synchronize external systems such as PIV or optical deformation measurements.

2.3. High-speed PIV system

A PIV system was used to capture the velocity distribution in an axial-radial slice plane through the rotor wake flow, see Fig. 3 (right). For tests with the DST geometry, a double-pulsed Nd:YLF laser (Quantronix Darwin Duo) was combined with a light sheet optics, illuminating the motion of aerosolized DEHS oil droplets serving as flow tracers within the measurement region. A sufficient seeding quality is challenging, since the laser's pulse energy of about $30\,\mathrm{mJ}$ is low, and since the non-recirculating inflow requires a large rate of tracer particle generation. The seeding devices comprised a single "two-fluid" generator (PIVcts1000) and three "Laskin-nozzle" generators (PIVpart). The latter type produces droplets with a diameter distribution around $1\,\mu\mathrm{m}$, about half the size of the former type[22]. Small droplets are important to reduce the size of the particle voids in the tip vortex centers, see Sec. 3.3 for details. The seeding generators were placed upstream of the wind tunnel's fan, resulting in a sufficiently homogenous distribution when approaching the rotor plane.

Two double-frame cameras (Phantom VEO 640) were mounted left and right below the test stand in a stereoscopic layout with an enclosed angle of about $90°$, providing instantaneous three-component velocity distributions after applying an iterative PIV cross-correlation algorithm (LaVision DaVis 8). The high-speed laser and cameras were phase-locked to the rotor and operated at 576 Hz, acquiring successive double-images with a rotational increment of $\Delta\Psi = 15°$. This allows to both track the tip vortices within a single rotor revolution, and to calculate flow statistics at a constant phase angle or wake age. For constant-pitch cases, 450 samples per phase angle were recorded.

For cases with cyclic swashplate settings, the phase of the pitch oscillation varies sinusoidally over the azimuth, with a constant pitch phase in the PIV region. Therefore, the swashplate can be slowly rotated around the rotor axis, similar to a helicopter turning along its vertical yaw axis. This varies the local pitch phase as seen in the stationary PIV region, and the entire pitch motion was recorded with about 1100 flow samples evenly distributed over the entire pitch cycle.

The reference data for the conventional PBT geometry was acquired during an earlier campaign with a very similar PIV setup, see Wolf et al.[41] for further details. It is noted that the results shown in this earlier publication consider a larger inflow velocity ($V_\infty = 4.4\,\mathrm{m/s}$) with a reduced rotor thrust, and, therefore, differ from the PBT results shown in the current work. The PBT experiments used a low-speed laser, only capturing a single PIV image every fourth revolution. Hence, data acquisition took significantly longer, but the same phase-locked rotor angles ensure a one-to-one comparison to the new DST test results at the same wake ages. Both data sets were evaluated with the same algorithms, and the grids provide a similar spatial resolution on the order of 1 mm or 1.4% chord.

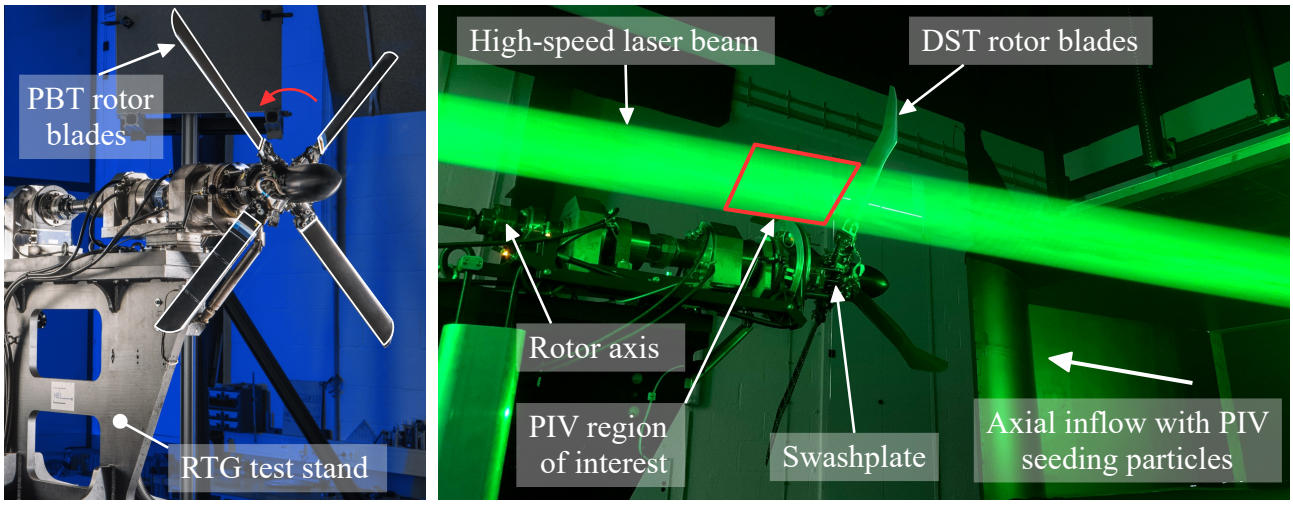

Figure 3: Frontal view of the RTG with parabolic-tip rotor blades (PBT, left), side view of the RTG with double-swept rotor blades (DST, right) during PIV operation.

3. RESULTS: STATIC PITCH ANGLES

3.1. Thrust polar and blade loading

Figure 4 shows the constant-pitch thrust polars of the conventional PBT and innovative DST geometries by means of the blade loading, C_T/σ, as a function of the root pitch angle, Θ. The thrust of the PBT geometry (×) increases linearly up to $\Theta = 28°$ and peaks at about $\Theta = 29°$, see label a). The double-swept geometry (○) results in a broad two-step stall behavior. A reduced but positive thrust slope, $dC_T/d\Theta$, starts at $\Theta \approx 25°$, see label b). The thrust maximum is reached much later at $\Theta = 34°$, see label c).

The interval between b) and c) goes along with a decreasing DST rotor efficiency (○) as seen by the figure of merit in Fig. 5. This is in contrast to a nearly constant PBT figure of merit (×) up to the PBT stall at a). The rotor power was measured by a torque sensor integrated into the RTG drive shaft, and the non-negligible friction of the bearings between sensor and rotor was compensated via tare measurements with removed rotor blades. The PBT-to-DST offset before reaching b) at $C_T/\sigma < 0.12$ is considered to be within the measurement uncertainty, but the qualitative trends in Fig. 5 are valid. It is noted that the blade inflow Mach number is too low for compressibility effects, and for a positive influence of the DST sweep angle on the rotor performance.

Earlier numerical studies by Kaufmann et al.[10] suggest that the two-step stall behavior of the DST geometry is caused by tip separation involving the tip vortex. This is confirmed by pressure-sensitive paint (PSP) data from Weiss et al.[36], see Fig. 6 for the pressure distribution C_pM^2 on the blade's upper surface. At $\Theta = 24°$ (top), the footprint of the tip vortex is a thin, streamwise low-pressure line at the very tip, and this result is qualitatively similar to Wong et al.'s[40] observations on the NASA PSP rotor.

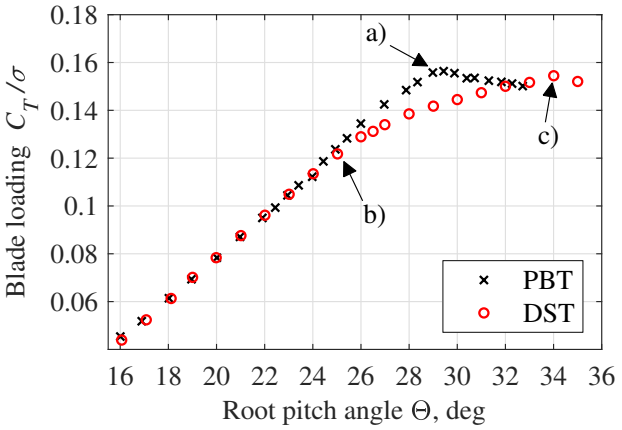

Figure 4: Blade loading versus pitch angle.

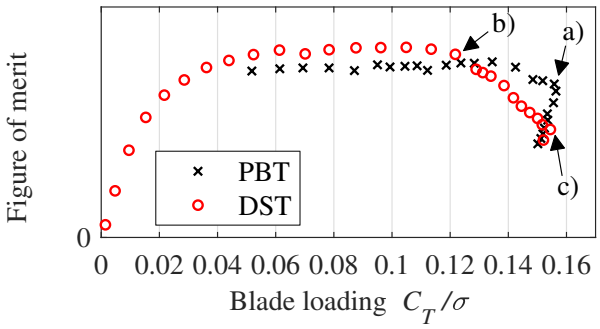

Figure 5: Figure of merit versus blade loading.

Increasing the blade pitch to $\Theta = 25°$ (Fig. 6, center) causes the tip vortex to jump in the inboard direction. Its footprint is now a broader, slanted lobe anchoring close the beginning of the leading edge's parabolic arc. A further increase of the blade pitch,

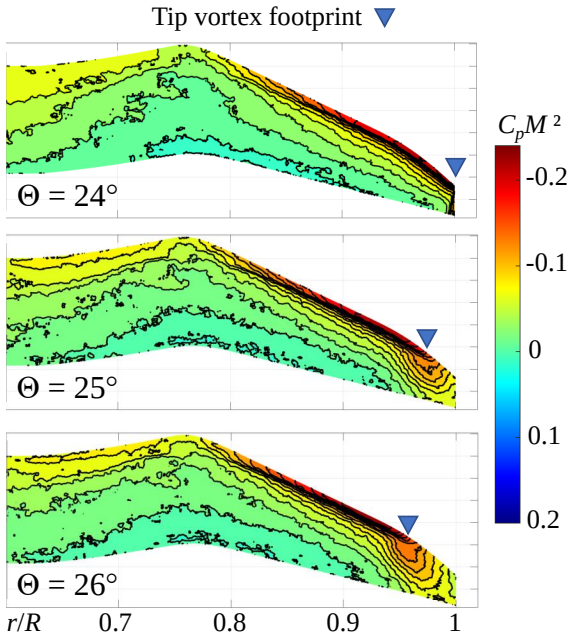

Figure 6: Pressure distribution on the blade's upper surface, data adapted from Weiss et al.[36].

for example to $\Theta = 26°$ (Fig. 6, bottom), continuously pushes the vortex footprint along the straight-edged backward-swept part of the tip, and in inboard direction.

This data supports the hypothesis that the backward sweep acts as a "delta wing"-like shape for $\Theta \geq 25°$. The vortex over the blade tip's upper surface effectively delays flow separation over the rest of the blade towards higher pitch angles, $\Theta \geq 34°$, at the cost of an increased drag in comparison to the "clean" airfoil flow for $\Theta < 25°$. The character of the tip flow is mirrored by the structure of the rotor wake, which will be shown in the next section.

3.2. Flowfield

Figure 7(a) shows an instantaneous flowfield in the wake of the DST rotor, taken with an azimuthal offset of $\Delta\Psi = 10°$ after the passage of blade number 2 of 4. The root pitch angle of $\Theta = 24°$ is constant and without cyclic input, hence, the inflow of the blades is steady. The main flow direction is left to right, and the coloring represents the horizontal velocity component u, normalized with the average velocity in the rotor plane after momentum theory in climb[14]:

$$(1)\quad V_\infty + V_i = \frac{V_\infty}{2} + \sqrt{\left(\frac{V_\infty}{2}\right)^2 + \frac{T}{2\rho A}} = 9.98\,\mathrm{m/s}$$

The rotor plane is at $x = 0$ as indicated by the vertical dashed line (**--**). The slipstream boundary separates the rotor wake in the lower part from the external flow in the upper part. The boundary is curved due to the wake contraction, and contains four tip vortices originating from the four rotor blades $2, 1, 4, 3$ (left to right). Hence, the local ages of the vortices are $\Psi_V = 10°, 100°, 190°, 280°$.

Figure 7(b) shows the phase-averaged and normalized out-of-plane vorticity ω, accounting for a total of 450 phase-locked samples. The four tip vortices appear as circular dots with a positive rotation. The youngest (leftmost) tip vortex blends into the corresponding blade shear layer, which at this age appears as a straight and vertical structure. The shear layer gradually transitions from counterclockwise rotation (yellow, upper part) to clockwise rotation (blue, lower part) in the radial region of the blade's thrust maximum, $y/R = 0.75 - 0.90$.

Figure. 7(c) corresponds to a later phase angle with $\Psi_V = 55°$ for the youngest tip vortex. The downstream motion of the wake structures depends on the local convection velocity and, hence, on the radial thrust distribution. The motion velocity of the shear layer is up to about twice the convection velocity of the tip vortices. Hence, the youngest (leftmost) shear layer has reached the preceding tip vortex created a quarter revolution earlier, with a beginning interaction of both structures.

Comparing Fig. 7(c) with Fig. 7(d) shows that the overall wake layout and the tip vortex structure of the DST and PBT geometries are very similar. The conventional blade shear layer has a single kink at about $y/R = 0.8$, corresponding to the local maximum of the spanwise thrust distribution. In contrast, the double-swept blade shear layer has two kinks at $y/R = 0.65$ and $y/R = 0.8$, approximately corresponding to the start of the forward-swept and backward-swept blade sections, and to the related changes in the thrust distribution. Despite an almost identical overall thrust level, the double-swept geometry initially deposits less vorticity in the tip vortex itself, but rather spreads a significant portion of trailing vorticity in a region further inboard. This can be seen from a comparison of the areas marked by red arrows in Figs. 7(c) and (d). Yamauchi et al.[43] and Potsdam et al.[20] reported a similar observation in a study of a full-scale UH-60A rotor with swept-back blade tips, creating two individual trailing vortices termed "tip vortex" and "planform vortex". It is noted that multi-vortex systems are well known from other planform or twist breaks, such as trim tabs, flaps, etc. However in the current case, the changes of the double-swept planform are too gradual to initiate a second individual planform vortex.

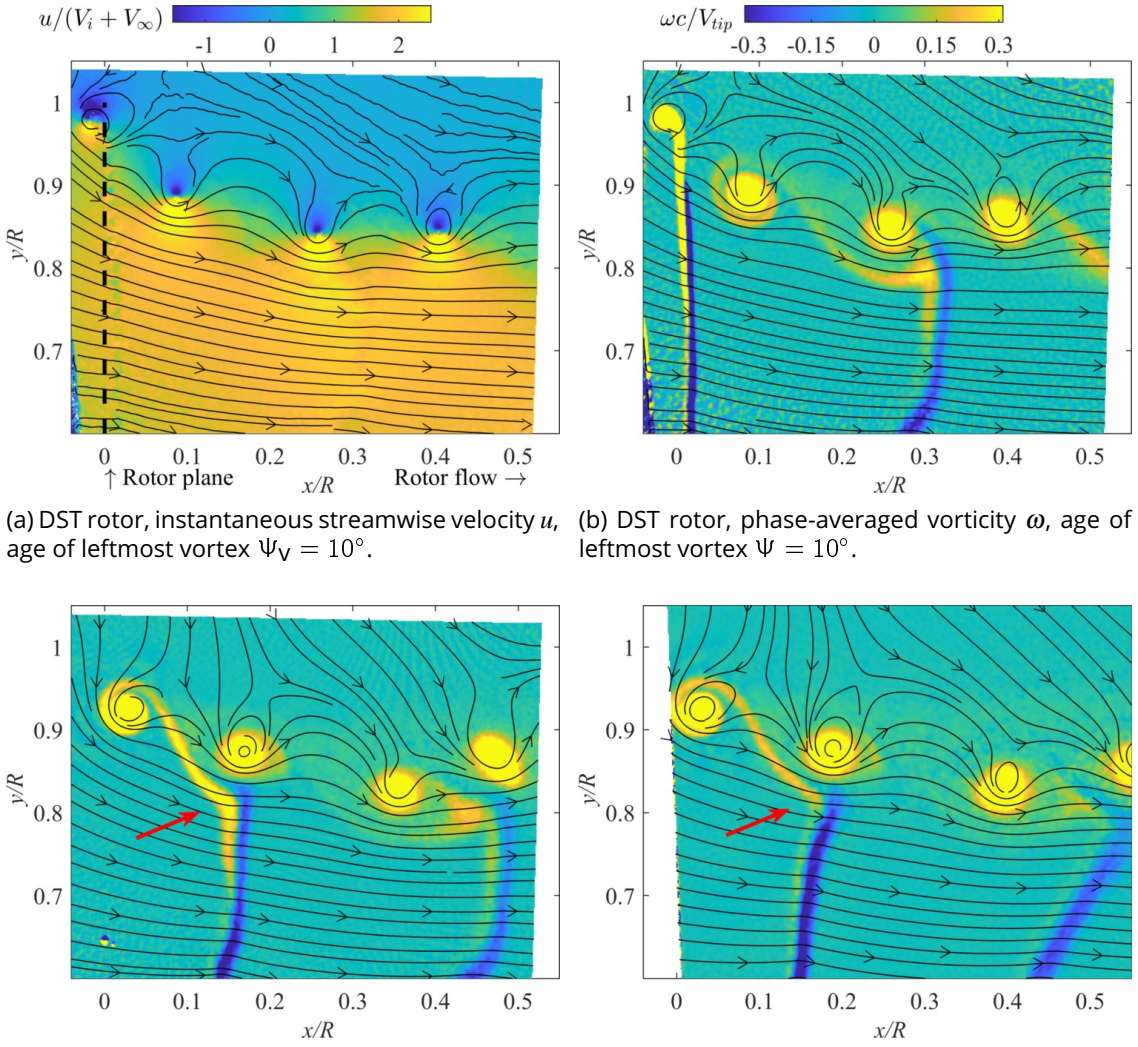

(a) DST rotor, instantaneous streamwise velocity u, age of leftmost vortex $\Psi_V = 10°$.

(b) DST rotor, phase-averaged vorticity ω, age of leftmost vortex $\Psi = 10°$.

(c) DST rotor, phase-averaged vorticity ω, age of leftmost vortex $\Psi = 55°$.

(d) PBT rotor, phase-averaged vorticity ω, age of leftmost vortex $\Psi = 55°$.

Figure 7: Sample PIV results of the rotor wake, blade root pitch angle $\Theta = 24°$.

3.3. Tip vortex structure and detection

The phase-averaged results in Figs. 7(b) to 7(d) cannot be used for detailed studies of the vortex structure, since they do not account for aperiodic jitter of the vortex centers and, hence, blur the velocity footprint. Instead, the vortex positions were identified in instantaneous flowfields, followed by calculating the shift-corrected "conditional average" at a given phase as defined by van der Wall and Richard[34] and adapted by later publications[11,23,24]. The current evaluation scheme was reused from earlier RTG studies[2,41], and is shown in Fig. 8 for PBT (left column) and DST (right column) sample tip vortices at $\Psi_V = 145°$. The out-of-plane vorticity ω, Fig. 8b, is low-pass filtered with a convolution kernel matched to the expected core size. The centroid of the filtered distribution (+) marks the vortex center.

A multitude of other identification schemes is available, for example, see Soto-Valle et al.[31] for a comprehensive review. The current PIV recordings, Fig. 8a, are affected by voids resulting from centrifugal forces acting on the flow tracer particles. In this situation, the "filtered vorticity"-approach was found to be particularly reliable for center detection[2].

The instantaneous velocity distributions are transformed into polar coordinates originating in the identified vortex centers. This yields the tangential (swirl) velocity as a function of the radial coordinate, $V_\theta(r)$, which is then averaged over all azimuthal directions and all flow samples at a given rotor phase. The result for the tip vortex aged $\Psi_V = 145°$ is shown in Fig. 9 (top) for both PBT and DST, corresponding to the second leftmost vortices in Figs. 7(c) and 7(d). The radial stepping matches the spatial resolution of the underlying PIV data. The PIV algorithm produces velocity data

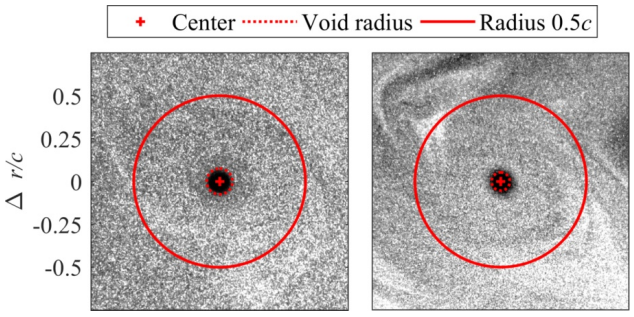

(a) PIV images.

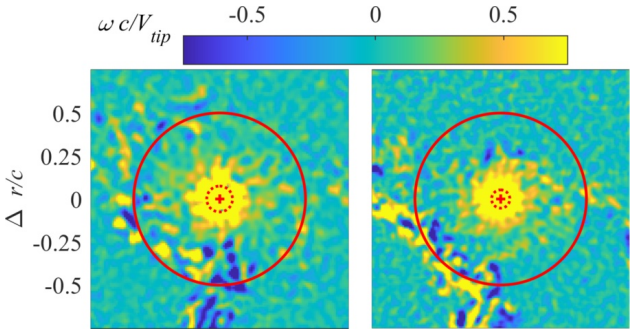

(b) Vorticity distributions, unfiltered.

Figure 8: Instaneous samples of the tip vortex at $\Psi_V = 145°$ for PBT (left) and DST (right).

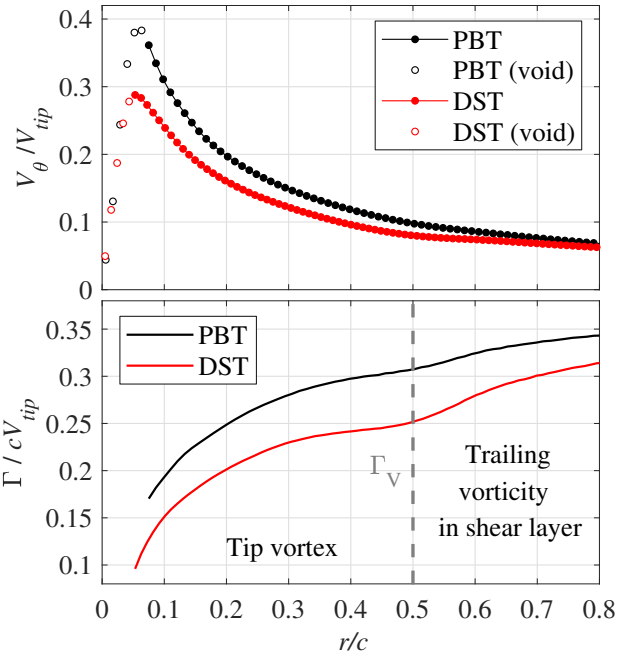

Figure 9: Conditional-averaged tangential velocity (top) and circulation (bottom) profiles of the tip vortex at $\Psi_V = 145°$.

even within the particle void due to the multi-pass approach. Automatic void masking is available within PIV processing, but in the current study, the voids are detected in a separate post-processing step based on the brightness levels in the raw camera images. Conditional-averaged velocity data is considered unreliable if 50% or less of the individual data is within the void region, as marked by unfilled symbols in Fig. 9 (top). The identified void agrees well with the visual impression of the raw camera images, see - - - in Fig. 8(a).

For $\Psi_V = 145°$ in Fig. 9 (top), the DST (•) produces tip vortices with lower V_θ compared to the PBT (•), about 22% less at $r = 0.1\ c$ despite comparable blade loadings. The reduced tangential velocity goes along with a smaller void radius (DST: 0.053 c, PBT: 0.075 c). It is noted that the void size is a function of the vortex history and not the local velocity distribution alone, see Domogalla[6] for further details.

Fig. 9 (bottom) shows the radial distribution of the vortex circulation Γ, calculated using the conditional-averaged swirl velocity via $\Gamma = 2\pi r V_\theta$. It is impossible to fully isolate individual tip vortices embedded in a complex flowfield with neighboring tip vortices and blade shear layers. Our preceding studies[2,7,41] used $\Gamma_V = \Gamma(r = 0.5\ c)$ as a substitute for the total circulation, which for an isolated vortex is defined at large radii, $r \to \infty$. Γ_V covers the most relevant area around the vortex center, for example, see Fig. 8 (—). The remaining circulation gradient, $d\Gamma/dr$, is comparably small, see the dips at $r = 0.5\ c$ (– –) in Fig. 9 (bottom). The circulation growth then re-increases due to an inclusion of trailing vorticity within the inboard blade shear layer, which has not been entrained into the tip vortex structure itself. This growth effect is stronger for the DST (—), whose overall circulation gradually closes the gap to the PBT (—). This supports the qualitative findings of the vorticity distributions, see the red arrows in Figs. 7(c) and 7(d). It is noted that the added shear layer-vorticity is aged $\Psi_V = 55°$ and originates from the successive blade passage, here approaching and passing the preceding tip vortex at $\Psi_V = 145°$.

3.4. Aperiodic variations, vortex pairing, and vortex trajectories

The DST-PBT comparison can be extended to higher vortex ages but requires caution due to "vortex pairing". This mechanism involves perturbations of the equidistant vortex spacing, and a subsequent orbital motion of vortices around each other due to mutually induced differential velocities. Vortex pairing has been reported in numerous rotor studies[3,4,26,29] and is known to cause or amplify vortex break-down. Initial stages of pairing are visible in Figs. 7(c) and 7(b) as out-of-line positions of the

rightmost vortices, but a better visualization is given in Fig. 10 by means of three vorticity snapshots in the PBT wake with a phase spacing of $\Delta\Psi = 45°$. The images were not taken during a single rotor revolution, but the overall process is periodic. The leapfrogging of the tip vortices trailed from blades 3 and 4 is obvious but only partly covered by the PIV field of view, both vortices cross the right edge at $x/R \approx 0.7$ almost simultaneously. Vortices 1 and 2 follow on similar pairing trajectories (not shown). The pairing results in a broadening of the wake's slipstream boundary and a production of small-scale turbulence.

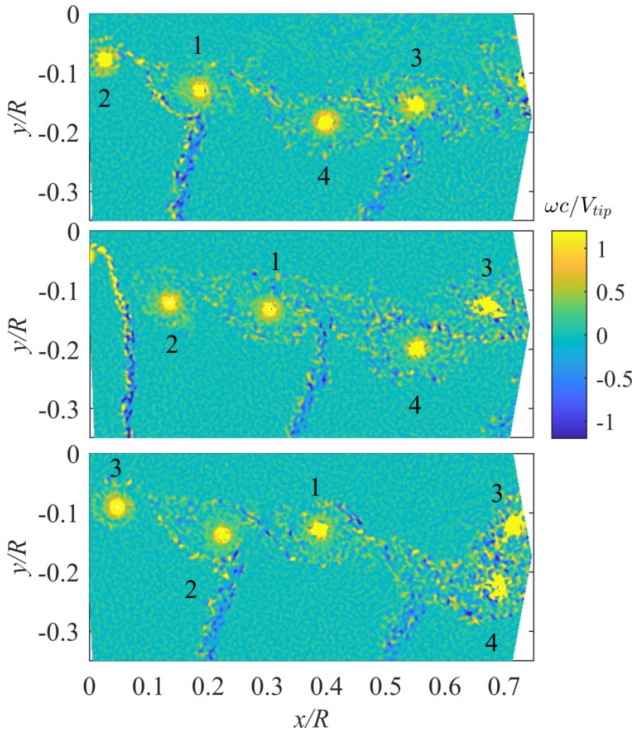

Figure 10: Pairing process of PBT blade tip vortices "3" and "4", $\Delta\Psi = 45°$ between successive images.

Pairing is attributed to small irregularities in the initial conditions[21], for example originating in the blade tracking or the blade pitch angles. Even though pairing can be considered an imperfection of the current test setup, it is a fundamental mechanism of rotor aerodynamics and also observed on free-flying helicopters[26,42]. For the PBT wake, the tip vortices of all four blades were tracked over almost an entire rotor revolution. Each phase-averaged data point in Fig. 11 accounts for 450 individual flow samples, covering ages between $\Psi_V = 40°$ and $\Psi_V = 340°$, and the resulting vortex trajectories clearly show a pairing-related split. Relative to the mean trajectory of all vortices (– –), vortices 1 (●) and 3 (■) are pushed in upstream and outboard direction, whereas vortices 2 (♦) and 4 (▲) move in downstream and inboard direction. Moreover, the split between vortices (1,2) is larger compared to vortices (3,4), indicating that both pairing processes are similar but not identical.

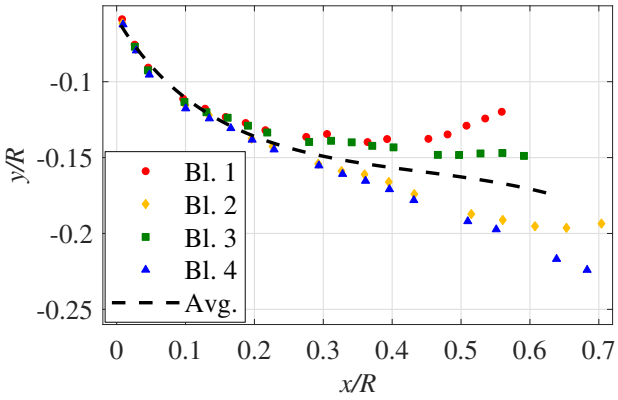

Figure 11: Average tip vortex trajectories, $\Psi_V = 40°$ to $\Psi_V = 340°$, for PBT blades 1 to 4.

Figure 12 compares the conditional-averaged V_θ-profiles of the tip vortices trailing blades 1 to 4 at $\Psi_V = 145°$ (top) and $\Psi_V = 325°$ (bottom). In the former case, the differences between individual blades are small, particularly in comparison to the much larger PBT/DST-related differences as in Fig. 9. In the latter case, all four tip vortices have aged, as seen by smaller maximum velocities and broader velocity profiles. The aging trend is much more pronounced for blade 2 (♦) and 4 (▲) in comparison to blade 1 (●). The mutual (1,2)-pairing affects both tip vortices simultaneously, but since vortex 2 is younger with a phase offset of $\Delta\Psi_V = -90°$, it is plausible that a pairing-related break-down starts earlier when observed as a function of the vortex age Ψ_V. Similar to the result of the vortex trajectories, the split of the (3,4)-pairing is similar to (1,2) but less pronounced.

The procedure was repeated for the entire PBT data set, and the maximum relative deviation of V_θ was determined for all pairwise blade combinations and within the valid (void-free) radial range. The result is shown in Fig. 13, giving a worst case-estimate of the blade-to-blade uncertainty at a given vortex age. For up to $\Psi_V = 300°$, the blade-to-blade differences are on a small and constant level with an average of about 6.2%. This result is significant since the pairing-related split of the vortex trajectories begins much earlier, at roughly about $\Psi_V = 145°$ or $x/R = 0.2$ in Fig. 11. For ages larger than $\Psi_V = 300°$, the deviation strongly increases to values exceeding 30%.

Experiments with the DST rotor did not track all four tip vortices over the entire age range due to time restrictions. Instead, the phase of the youngest vortex 2 was varied between $10°$ and $70°$, with older

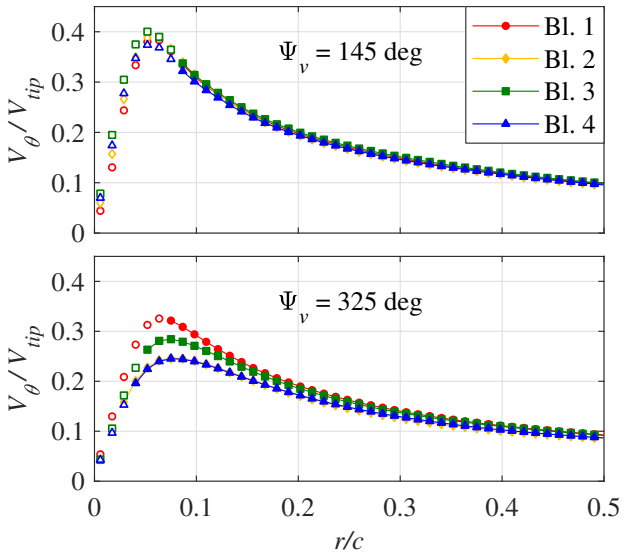

Figure 12: Conditional-averaged tangential velocity profiles, $\Psi_V = 145°$ (top) and $\Psi_V = 325°$ (bottom).

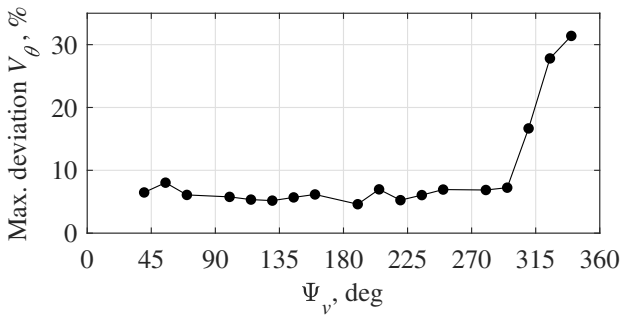

Figure 13: Maximum relative difference of V_θ between any combination of PBT blades 1-4.

ages covered by the vortex (blade) sequence 2,1,4,3 as in Figs. 7(b) and 7(c). Figure 14 shows the trajectory's phase-averaged streamwise component, x, taken from all four vortices. A small discontinuity between blades 4 and 3, see the black arrow marker, results from the onset of vortex pairing. Nevertheless, a polynomial data fit (– –) shows that the DST vortices move slower in the downstream direction compared to the PBT reference blade (– –, data repeated from Fig. 11).

This observation corresponds to the discussion of the tip vortex strength: At a given C_T/σ, the DST geometry relocates thrust in inboard direction, which not only weakens the tip vortex, but also reduces the local downwash velocity and, hence, the vortex convection. It is noted that the DST vortex trajectory in Fig. 14 begins at slightly negative x-values. This is due to the tip vortices forming on the suction side of the rotor blades, and due to the fact that the nominal position of the rotor plane ($x = 0$) does not account for blade bending during operation.

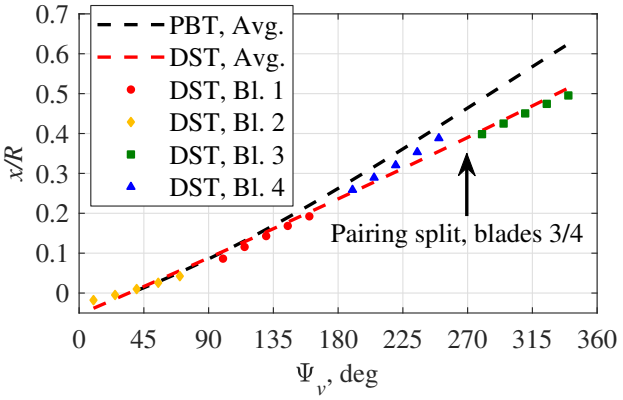

Figure 14: Streamwise tip vortex convection motion for DST and PBT blade geometries.

3.5. Blade geometry and vortex structure

Figure 15(a) shows the evolution of the tip vortex circulation Γ_V as a function of the vortex age Ψ_V for both PBT (•) and DST (•) blade geometries. PBT results are only available for $\Psi_V \geq 100°$ (green arrow marker), since the younger tip vortices were too close to the left border of the PIV field of view. This shortcoming was eliminated in the later DST experiments by a slight repositioning of the PIV cameras. Nevertheless, it is confirmed that the PBT geometry deposits a larger share of the entire trailing vorticity within the tip vortex region. By tendency, the circulation of both geometries decreases over Ψ_V due to the aging processes, and this loss is not compensated by an entrainment of additional shear layer-vorticity passing nearby.

The stronger PBT tip vortices are accompanied by a larger maximum tangential velocity V_θ, see Fig. 15(b), although some of the PBT data is considered unreliable due to the particle void (unfilled symbols). Within $70° \leq \Psi_V \leq 100°$, there is an odd discontinuity in the DST data (blue arrow marker). The maximum swirl velocity jumps up by about 50%, contrary to the general aging trend, and despite an almost constant circulation level. This is unlikely due to an aerodynamic recombination/relaminarization process of the tip vortex, but more probably, due to blade-to-blade variations and the underlying switch from blade "2" to blade "1". However, the pairing-related blade-to-blade uncertainties were found to be much lower.

The current root pitch angle of $\Theta = 24°$ is below but close to the first kink in the C_T-polar, see label a) in Fig. 4 and corresponding discussion. Hence, two additional DST constant-pitch cases with a thrust variation of about $\pm 10\%$ were evaluated, see Tab. 1. For "DST-high", the thrust was increased via an increased blade pitch angle, whereas "DST-low" used

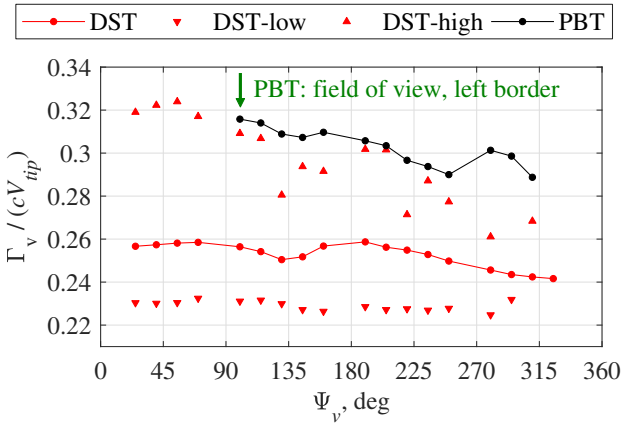

(a) Tip vortex circulation.

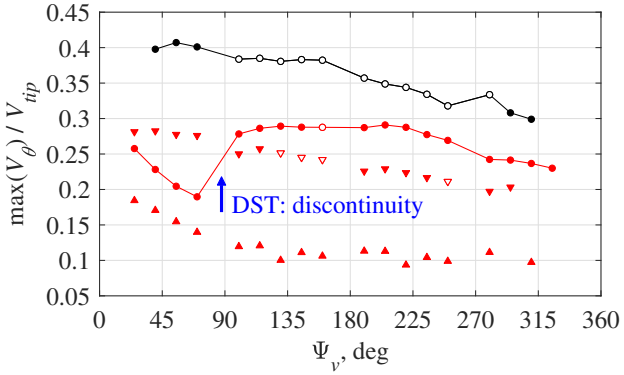

(b) Maximum tangential velocity, unfilled symbols: values within particle void.

Figure 15: Evolution of tip vortex parameters over vortex age Ψ_V.

an increased axial inflow velocity V_∞ to reduce the blades' aerodynamic angle of attack.

Case	DST	DST-low	DST-high	PBT
C_T/σ	0.115	0.103	0.127	0.119
Θ	24°	24°	26°	24°
V_∞	2.2 m/s	4.4 m/s	2.2 m/s	2.2 m/s

Table 1: Parameters of the test cases in this section.

The thrust variation affects the tip vortex circulation as expected, see Fig. 15(a): a larger thrust yields a larger circulation and vice versa. However, the DST-high case (▲) starts on a disproportionately large Γ_V-level at young ages, and decreases faster over Ψ_V, including a larger scatter. Against expectations, the DST-low case (▼) produces tip vortices with higher maximum tangential velocities in comparison to the DST-high case (▲), see Fig. 15(b). This means that the tip vortices of both cases are not self-similar and structurally different. It is noted that the DST-high case is similar to the DST case (•) at young ages, $0 \leq \Psi_V \leq 90°$, but continues the trend at higher ages without any discontinuity.

The results suggest that the tip vortex undergoes a structural change related to the different radial anchor positions as seen in the PSP images, Fig. 6, and the corresponding kink in the thrust polar. This structural change is visible when looking at instantaneous flow samples, for example, the vorticity distributions of the tip vortices at $\Psi_V = 55°$ and $\Psi_V = 145°$. The DST-high flowfield in Fig. 16(b) is strongly influenced by small-scale turbulent structures with both counter-clockwise and clockwise senses of rotation (blue and yellow areas), despite having a larger counter-clockwise net circulation compared to the DST-low case in Fig. 16 (a).

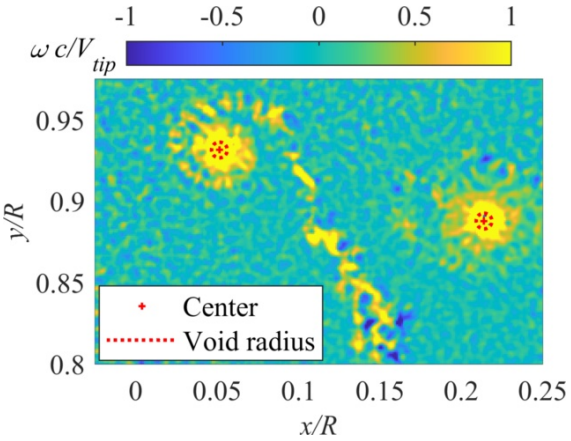

(a) DST-low, $C_T/\sigma = 0.103$.

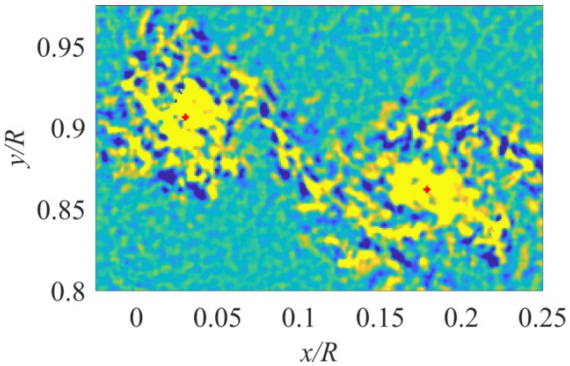

(b) DST-high, $C_T/\sigma = 0.127$.

Figure 16: Instantaneous samples of the out-of-plane vorticity ω, age of leftmost vortex $\Psi_V = 55°$.

The turbulence also results in an increased mixing along the vortex radius and, therefore, eliminates the tracer particle void (- - -), which is only detected in the DST-low case but not in the DST-high case. The absence of a void means that the DST-high PIV result is reliable even in the inner core area.

Figure 17 shows the phase-averaged radial positions, y, of young tip vortices as a function of the vor-

tex age. Both DST-low and DST-high vortices move in inboard direction due to the vortex roll-up and the wake contraction, but the DST-high vortex at $\Psi_V = 10°$ starts in a more inboard position, $y/R = 0.966$ versus $y/R = 0.984$ for DST-low. This supports the PSP findings in Fig. 6, which imply that the DST-high vortex anchors further inboard along the leading edge rather than at the tip itself. The DST-high standard deviation of the y-position, represented by error bars in Fig. 17, is increased by a factor of seven and more in comparison to DST-low, which underlines the impact of unsteadiness and turbulence.

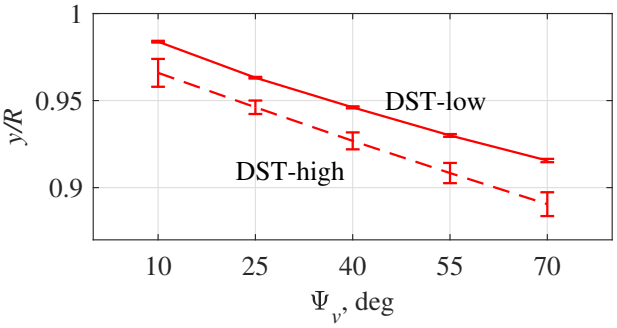

Figure 17: Phase-averaged radial positions of young tip vortices, with standard deviation as errorbars.

The strongest change in the vortex structure was observed in the vortices' axial velocity, which is shown by the phase-averaged out-of-plane w-component in Fig. 18. In the non-rotating coordinate system, negative (blue) colors represent a wake or velocity deficit, whereas positive (yellow) colors represent a jet against the blade's motion direction.

In the DST-low case in Fig. 18(a), the blade's wake is visible as a spiraling light-blue structure wrapping around the left tip vortex. The region close to the vortex center shows an alternating pattern with a wake on the blade's upper (left) side, but a jet on the blade's lower (right) side. Jet-like structures in the vicinity of rotor tip vortices were reported before [12]. A recent study [30] on wingtip vortices observed a jet region very similar to the current pattern in Fig. 18(a), and explained this "velocity excess" as a result of the narrowing flow channel between tip vortex and shear layer.

The DST-high case produces a very different pattern with large velocity deficits in the tip vortex regions, see the dark-blue areas in Fig. 18(b). A velocity deficit and the corresponding impulse transfer from blade to fluid indicates a larger blade drag, which qualitatively agrees with the reduced figure of merit for $\Theta > 24°$ in Fig. 5. The minimum levels at $\Psi_V = 0.55°$ are below $w/V_{tip} = -0.2$.

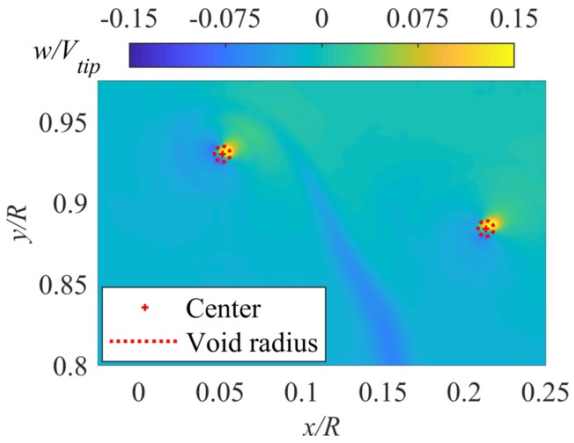

(a) DST-low

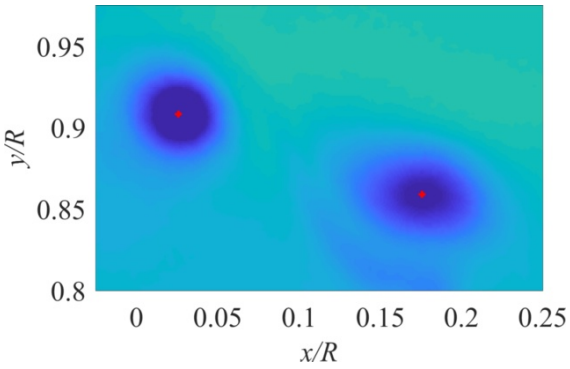

(b) DST-high

Figure 18: Phase-averaged out-of-plane velocity component w, age of leftmost vortex $\Psi_V = 55°$.

4. RESULTS: PITCH OSCILLATIONS

The behavior of the tip flow was also studied in test cases with cyclic swashplate input and, hence, a sinusoidal pitch motion. The unsteady inflow of the blades is similar to a trimmed helicopter main rotor in forward flight, but the RTG test stand only provides axial inflow without an edgewise velocity component. The following test case considers an oscillation described by

$$\Theta = 24° - 6° \cos(2\pi t f).$$

This notation is abbreviated to "$24° \pm 6°$" in the following. The mean angle of the pitch oscillation matches the constant-pitch reference case in the preceding section. The pitch peak at $30°$ is slightly above the constant-pitch PBT thrust maximum at $29°$, but well below the constant-pitch DST thrust maximum at $34°$ (Fig. 4). It is noted that the individual pitch signals of the four rotor blades as measured by Hall sensors differ by up to $\pm 0.2°$ from the stated nominal values, which is the error margin of the RTG swashplate adjustment particularly under dynamic loads with cyclic input.

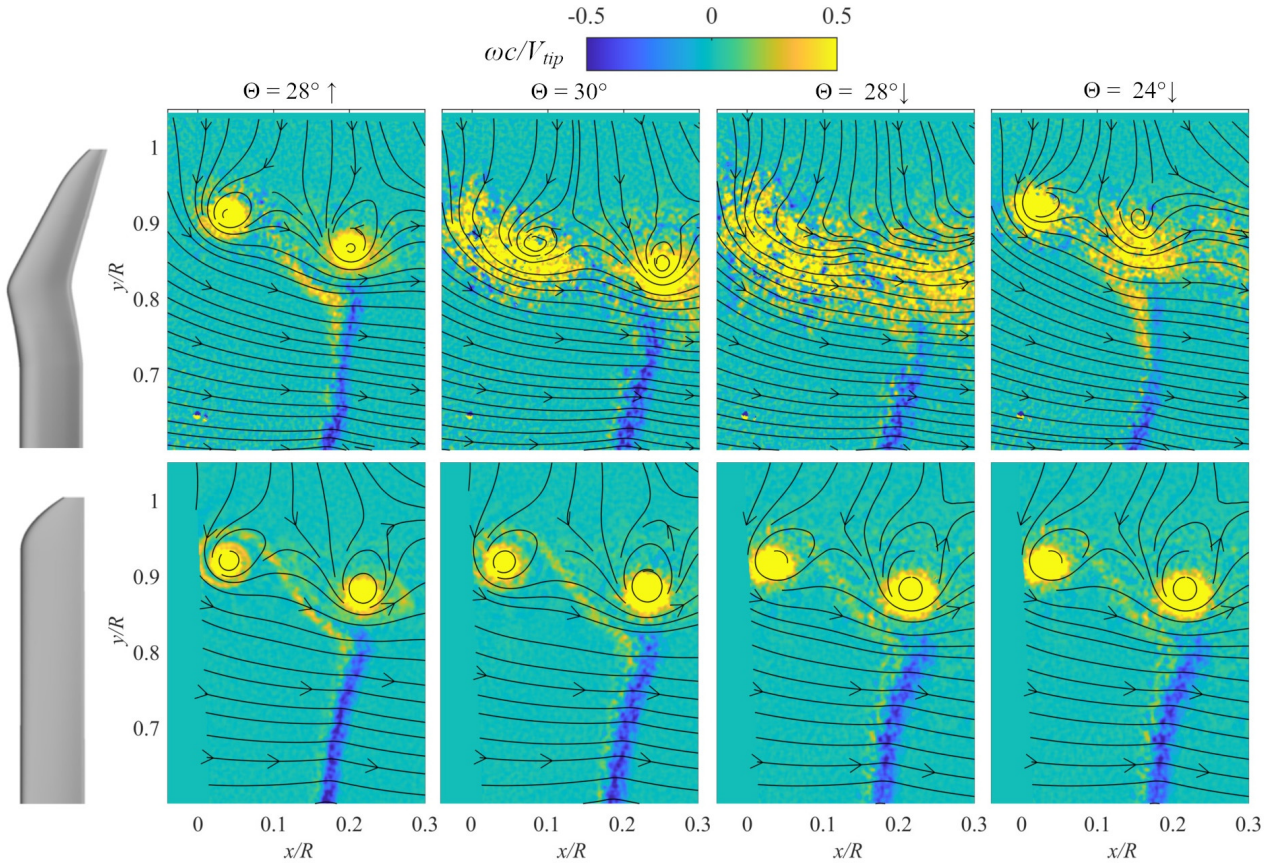

Figure 19: DST (top) and PBT (bottom) wake for pitch motion $\Theta = 24° \pm 6°$, averaged in windows sized $\pm 1\%$ of the cycle, mean blade pitch $\Theta = 28° \uparrow, 30°, 28° \downarrow, 24° \downarrow$, youngest (leftmost) tip vortex at $\Psi_V = 55°$.

Figure 19 shows the sliding phase-averaged vorticity distributions, limited to the two youngest tip vortices at $\Psi_V = 55°$ and $\Psi_V = 145°$ for reasons of clarity. Left column to right column, the cyclic pitch phases were chosen so that the instantaneous blade pitch angles when crossing the PIV plane were $28° \uparrow$ (upstroke), $30°$ (maximum), $28° \downarrow$, and $24° \downarrow$ (both downstroke). The pitch phase slowly sweeps through the PIV plane during each test point due to the rotation of the swashplate, hence, each of the approximately 1100 PIV records has a unique and slowly increasing pitch phase angle. In this context, "sliding phase-averaged" means that 22 images within a phase window stretching $\pm 1\%$ of the cycle were averaged, with the stated nominal phase in the center of the window.

The conventional PBT geometry (bottom row in Fig. 19) produces in a "regular" wake structure with individual and well-separated blade tip vortices. Wolf et al.[41] used a similar pitch motion with a higher inflow velocity as a reference case* for PBT oscillations in fully attached flow conditions without separation. It was shown that except for hysteresis effects, the flow field and parameters of the tip vortices match the respective constant-pitch conditions.

In contrast, the DST geometry (top row) suffers from massive flow separation in the blade tip region, which is particularly visible at $\Theta = 28° \downarrow$ (third column). The individual blade tip vortices are replaced by a wavy streamline pattern and a broad vorticity layer stretching from $y/R = 0.8$ to $y/R = 0.9$. Despite averaging, the distribution is not smooth but affected by the footprints of individual small-scale structures. The predominant rotational sense of the trailed vorticity remains counter-clockwise (yellow coloring), corresponding to the continuing generation of thrust. The measured average blade loading for the pitch-oscillating DST and PBT geometries is nearly identical, $C_T/\sigma = 0.110$, and close to but below the constant-pitch values at $\Theta = 24°$ (Tab. 1). Additional details are given in Fig. 20, revisiting the phase-averaged DST wake at $\Theta = 30°$ (left) and $\Theta = 28° \downarrow$ (right) for an earlier wake age of $\Psi_V = 10°$, shortly after the passage of the rotor blade through the PIV plane. The blade's shear layer maintains a thin and straight outline up to about

*See "case 2" in Wolf et al.[41]. The latter publication states the pitch angle at 75% R, which is offset by $-6.9°$ to the root pitch angle stated in the current work due to the PBT's linear twist.

$y/R = 0.85$. Further outboard, the wake of the flow separation on the blade's suction side is visible as a large and turbulent vorticity blob, which strongly affects the further development of the rotor wake. In case of $\Theta = 30°$, the contained vorticity will eventually roll up into an individual but broad tip vortex, here visible for the preceding vortex at $\Psi_V = 100°$ in the center of Fig. 20 (left). For $\Theta = 28° \downarrow$ in Fig. 20 (right), this roll-up is no longer observed, only leaving a streamwise turbulent band which masks individual blade passes.

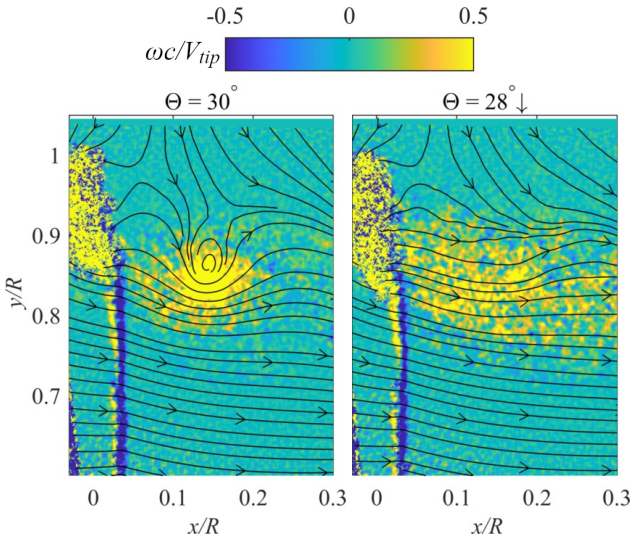

Figure 20: Phase-averaged DST wake, $\Theta = 24° \pm 6°$, youngest (leftmost) wake age $\Psi_V = 10°$.

A deeper insight into the wake hysteresis under pitch oscillations is given in Fig. 21, showing the conditional-averaged tangential velocity profiles at an age of $\Psi_V = 55°$. During the upstroke, the tip vortex conserves high maximum V_θ-levels around $0.3\ V_{tip}$ for $\Theta = 24° - 27°$, before gradually decreasing at $\Theta = 28°$. This is a distinct difference to the constant-pitch results, where a change in the vortex structure with a V_θ-drop of almost 50% at about $\Theta = 25°$ was observed, see Fig. 15 and the discussion of the kink b) in the thrust polar, Fig. 4. This shows that the time constant required for the tip vortex to switch between both states is non-negligible in comparison to the current pitch period of $1/24$ Hz $= 41.7$ ms.

Figure 21 also compares the V_θ-profiles at $\Theta = 24°$ for the upstroke (▲) and downstroke (▼). The hysteresis is very apparent, with the downstroke tip vortex not having recovered from the flow separation. The V_θ-profile is very broad and barely exceeds $0.1\ V_{tip}$. However, the V_θ-level at the radius $r/c = 0.5$ is almost identical to the upstroke, also resulting in a similar vortex circulation Γ_V.

Figure 22 shows the results at $\Psi_V = 10°$ for two

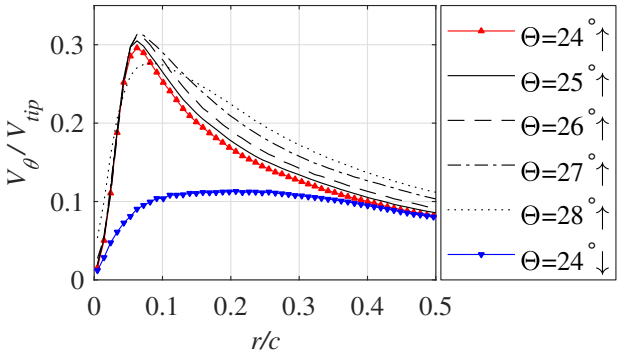

Figure 21: Sliding conditional-averaged tangential velocity profiles, $\Theta = 24° \pm 6°$, $\Psi_V = 55°$.

additional test cases with increased average pitch angles of $\Theta = 28°$ (left) and $\Theta = 30°$ (right) at a constant pitch amplitude of 6°. Both test cases maintain a large average blade loading, $C_T/\sigma = 0.133$ and $C_T/\sigma = 0.139$. The shown pitch phases were chosen so that the blade pitch angles in the PIV plane, $\Theta = 34°$ and $\Theta = 36°$, are at the respective pitch maximum. This enables a comparison between Fig. 20 (left) and Fig. 22 (left and right).

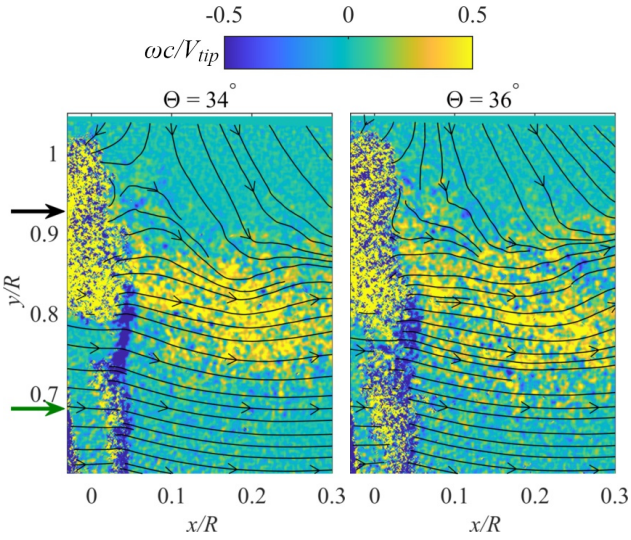

Figure 22: Phase-averaged DST wake, $\Theta = 28° \pm 6°$ (left) and $\Theta = 30° \pm 6°$ (right), $\Psi_V = 10°$.

Comparing Fig. 22 (left) to Fig. 20 (left), the increased average pitch angle yields a larger separated flow area over the outboard, backward-swept part of the blade ($y/R > 0.76$, see the black arrow). Furthermore, a second separated region forms in the inboard, forward-swept part of the blade ($0.63 < y/R < 0.76$, see the green arrow). CFD simulations of the current test setup and for the same pitch amplitude, see Kaufmann et al.[10], predict a similar double-separation structure. This is shown in Fig. 23 (bottom) for a maximum pitch angle

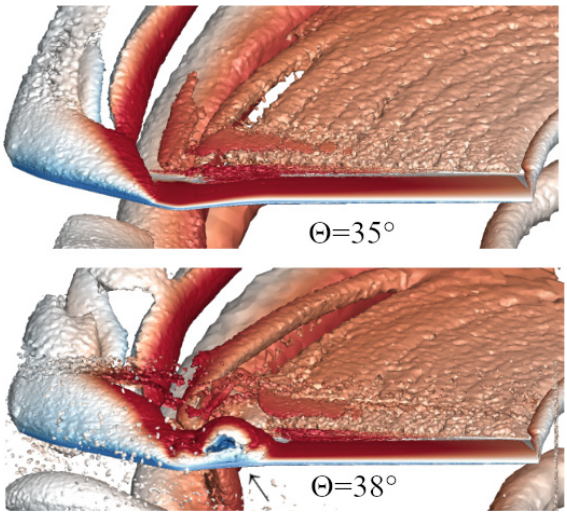

Figure 23: CFD results, adapted from Kaufmann et al.[10], λ_2-isosurfaces at the maximum pitch angles for oscillations with 6° amplitude.

of $\Theta = 38^\circ$. Kaufmann et al. showed that in addition to the separated tip vortex over the backward-swept tip part, which is already visible at $\Theta = 35^\circ$ (Fig. 23, top), the inboard separation over the forward-swept tip part is initiated by an Ω-like dynamic stall vortex. Further increasing the average pitch angle in the experiments, see Fig. 22 (right), yields increasing sizes of both separations until merging at the kink between the forward- and backward-sweep.

5. Conclusions

The structure of the tip vortex system in the wake of a four-bladed model rotor was studied at the rotor test stand Göttingen by means of particle image velocimetry. A double-swept tip geometry (DST) inspired by the ERATO rotor blade design was compared to a conventional reference design with a parabolic blade tip (PBT). The main results are summarized as follows:

- The DST tip planform results in a single tip vortex without forming additional planform-induced trailing vortices.
- For constant-pitch cases and at the same blade loading, the DST deposits less trailing vorticity in the tip vortex region itself, also resulting in smaller maximum tangential velocities and a smaller vortex spacing compared to the PBT. The remaining DST vorticity is shifted in inboard direction and contained in the blades' shear layers, which is not entrained into the corresponding tip vortex but passes preceding tip vortices due to a higher downstream convection velocity.
- The tip vortex systems of both DST and PBT are prone to the vortex pairing-instability, resulting in an accelerated vortex break-down. The pairing process begins with a split in the vortex trajectories trailing from different blades. A split in the tangential velocity profiles follows further downstream, accounting for larger blade-to-blade differences.
- The DST rotor has a two-step stall behavior, in which the first step is accompanied by a reduced but still increasing thrust slope. This event is connected to a sudden, structural change of the tip vortex structure. The vortex moves from the outmost blade tip region in inboard direction, and to a position over the upper side of the backward-swept blade section. This change is supported by earlier PSP results of the vortex footprint, and accompanied by a much larger cycle-to-cycle unsteadiness, a significantly lower tangential velocity, and a pronounced wake-like axial velocity matching the reduced rotor efficiency. However in constant-pitch tests, this flow configuration is stable enough to persist over a large pitch range, before reaching the second stall step and the maximum thrust level about $\Delta\Theta = 9^\circ$ later.
- DST test cases with sinusoidal pitch oscillations resulted in a hysteresis between the up- and downstroke. During the upstroke, structural changes of the tip vortex are delayed towards higher pitch angles. Sudden tip stall in the backward-swept region then initiates an entire break-down of the wake's tip vortex system, which is replaced by a turbulent band of trailed vorticity without large-scale vortical structures.
- Dynamic tip stall started at average blade pitch angles for which the flow over the conventional PBT geometry remained fully attached. However, the average thrust levels of DST and PBT are similar, underlining the gradual DST stall behavior, similar to a delta wing.
- A further increase of the average DST pitch angle yields a second separated region over the inboard forward-swept part, confirming earlier CFD simulations. Both separation regions grow with increasing pitch angle until merging at the forward-backward sweep kink of the DST planform.

6. Acknowledgments

The studies were conducted as a part of the DLR project "URBAN-Rescue". The authors would like to thank Markus Krebs for his support during the test campaign, Armin Weiss for contributing his PSP results, and Kurt Kaufmann for sharing his CFD data.

References

[1] Bhagwat, M. J., Leishman, J. G.: "Correlation of Helicopter Rotor Tip Vortex Measurements", *AIAA Journal* **38** (2), 2000. https://doi.org/10.2514/2.957.

[2] Braukmann, J. N., Wolf, C. C., Goerttler, A., Raffel, M.: "Blade Tip Vortex System of a Rotor with Cyclic Pitch", *AIAA Journal* **58** (7), 2020. https://doi.org/10.2514/1.J058678.

[3] Caradonna, F.: "Performance Measurement and Wake Characteristics of a Model Rotor in Axial Flight", *Journal of the American Helicopter Society*, **44** (2), 1999. https://doi.org/10.4050/JAHS.44.101.

[4] Chung, K., Hwang, C., Lee, D., Yim, J.: "Numerical Investigation on a Rotor Tip-Vortex Instability in Very Low Advance Ratio Flight", *International Journal of Aeronautical and Space Sciences* **6** (2), 2005. https://doi.org/10.5139/IJASS.2005.6.2.084.

[5] Dietz, M., Keßler, M., Krämer, E., Wagner, S.: "Tip Vortex Conservation on a Helicopter Main Rotor Using Vortex-Adapted Chimera Grids", *AIAA Journal* **45** (8), 2007. https://doi.org/10.2514/1.28643.

[6] Domogalla, V.: "Quantification of the Influence of Particle Voids on PIV Measurements via Synthetic-PIV", *Notes on Numerical Fluid Mechanics and Multidisciplinary Design* **151**, 2021. https://doi.org/10.1007/978-3-030-79561-0_31.

[7] Goerttler, A., Braukmann, J. N., Wolf, C. C., Gardner, A. D., Raffel, M.: "Blade Tip-Vortices of a Four-Bladed Rotor with Axial Inflow", *Journal of the American Helicopter Society* **65** (4), 2020. https://doi.org/10.4050/JAHS.65.042002.

[8] Harrison, R., Stacey, S., Hansford, B.: "BERP IV - The Design, Development and Testing of an Advanced Rotor Blade", 64th Annual Forum of the American Helicopter Society, Montréal, Canada, Apr 29–May 1, 2008.

[9] Jain, R.: "Sensitivity Study of High-Fidelity Hover Predictions on the Sikorsky S-76 Rotor", *Journal of Aircraft* **55** (1), 2018. https://doi.org/10.2514/1.C034076.

[10] Kaufmann, K., Müller, M. M., Gardner, A. D.: "Dynamic Stall Computations of Double-Swept Rotor Blades", *Notes on Numerical Fluid Mechanics and Multidisciplinary Design* **143**, 2020. https://doi.org/10.1007/978-3-030-25253-3_34.

[11] Kindler, K., Mulleners, K., Richard, H. van der Wall, B. G.: "Aperiodicity in the Near Field of Full-Scale Rotor Blade Tip Vortices", *Experiments in Fluids* **50** (6), 2011. https://doi.org/10.1007/s00348-010-1016-8.

[12] Komerath, N., Wong, O., Ganesh, B.: "On the Formation and Decay of Rotor Blade Tip Vortices", 34th AIAA Fluid Dynamics Conference and Exhibit, Portland, OR, USA, Jun 28–Jul 1, 2004. https://doi.org/10.2514/6.2004-2431.

[13] Kumar, M. R., Lokeswara, R. V.: "Aeroelastic Analysis of Double-Swept Rotor Blade in Hovering Conditions", International Forum on Aeroelasticity and Structural Dynamics, Como, Italy, Jun 25–28, 2017.

[14] Leishman, J. G.: *Principles of Helicopter Aerodynamics*, 2nd edition, Cambridge University Press, New York, NY, USA, 2006. Chapter 2.13 "Momentum Analysis in Axial Climb and Descent".

[15] Lütke, B., Nuhn, J., Govers, Y., Schmidt, M.: "Design of a Rotor Blade Tip for the Investigation of Dynamic Stall in the Transonic Wind-Tunnel Göttingen", *The Aeronautical Journal* **120** (1232), 2016. https://doi.org/10.1017/aer.2016.74.

[16] Müller, M. M., Schwermer, T., Mai, H., Stieg, C.: "Development of an innovative Double-Swept Rotor Blade Tip for the Rotor Test Facility Göttingen", Deutscher Luft- und Raumfahrtkongress, Friedrichshafen, Germany, Sept. 4-6, 2018.

[17] Müller, M., Weiss, A., Braukmann, J.N.: "Dynamic Stall Investigation on a Rotating Semi-Elastic Double-Swept Rotor Blade at the Rotor Test Facility Göttingen", 78th Annual Forum of the Vertical Flight Society, Ft. Worth, TX, USA, May 10–12, 2022.

[18] Mztourist, "H160 Tail showing biplane stabiliser, canted fenestron and rotor tip", image published at Wikimedia Commons under Creative Commons 4.0. https://commons.wikimedia.org/wiki/File:H160_Tail.JPG.

[19] Perry, F. J.: "Aerodynamics of the Helicopter World Speed Record", 43rd Annual National Forum of the American Helicopter Society, St. Louis, MO, USA, May 18–20, 1987.

[20] Potsdam, M., Jayaraman, B.: "UH-60A Rotor Tip Vortex Prediction and Comparison to Full-Scale Wind Tunnel Measurements", 70th Annual Forum of the American Helicopter Society, Montréal, Canada, May 20–22, 2014.

[21] Quaranta, H. U., Bolnot, H., Leweke, T.: "Long-Wave Instability of Helical Vortices", *Journal of Fluid Mechanics* **780**, 2015. https://doi.org/10.1017/jfm.2015.479.

[22] Raffel, M., Willert, C. E., Scarano, F., Kähler, C. J., Wereley, S. T., Kompenhans, J.: *Particle Image Velocimetry - A Practical Guide*, 3rd edition, Springer, Cham, Switzerland, 2018. Chapter 2.2.2 "Seeding of Gases". https://doi.org/10.1007/978-3-319-68852-7 (eBook).

[23] Ramasamy, M., Johnson, B., Leishman, J. G.: "Turbulent Tip Vortex Measurements Using Dual-Plane Stereoscopic Particle Image Velocimetry", *AIAA Journal* **47** (8), 2009. https://doi.org/10.2514/1.39202.

[24] Ramasamy, M., Paetzel, R., Bhagwat, M. J.: "Aperiodicity Correction for Rotor Tip Vortex Measurements", 67th Annual Forum of the American Helicopter Society, Virginia Beach, VA, USA, May 3–5, 2011.

[25] Schwarz, C., Bauknecht, A., Wolf, C. C., Coyle, A., Raffel, M.: "A Full-Scale Rotor-Wake Investigation of a Free-Flying Helicopter in Ground Effect using BOS and PIV", *Journal of the American Helicopter Society*, **65** (3), 2020. https://doi.org/10.4050/JAHS.65.032007.

[26] Schwarz, C., Bodling, A., Wolf, C. C., Brinkema, R., Potsdam, M., Gardner, A. D.: "Development of Secondary Vortex Structures in Rotor Wakes", *Experiments in Fluids* **63** (4), 2022. https://doi.org/10.1007/s00348-021-03348-8.

[27] Schwermer, T., Richter, K., Raffel, M.: "Development of a Rotor Test Facility for the Investigation of Dynamic Stall", *New Results in Numerical and Experimental Fluid Mechanics* **X**, 2016. https://doi.org/10.1007/978-3-319-27279-5_58.

[28] Schwermer, T., Gardner, A. D., Raffel, M.: "A Novel Experiment to Understand the Dynamic Stall Phenomenon in Rotor Axial Flight", *Journal of the American Helicopter Society* **64** (1), 2019. https://doi.org/10.4050/JAHS.64.012004.

[29] Sherry, M., Nemes, A., Lo Jacono, D., Blackburn, H. M., Sheridan, J.: "The Interaction of Helical Tip and Root Vortices in a Wind Turbine Wake", *Physics of Fluids* **25** (11), 2013. https://doi.org/10.1063/1.4824734.

[30] Skinner, S. N., Green, R. B., Zare-Behtash, H.: "Wingtip Vortex Structure in the Near-Field of Swept-Tapered Wings", *Physics of Fluids* **32**, 2020. https://doi.org/10.1063/5.0016353.

[31] Soto-Valle, R., Cioni, S., Bartholomay, S., Manolesos, M., Nayeri, C. N., Bianchini, A., Paschereit, C. O.: "Vortex Identification Methods Applied to Wind Turbine Tip Vortices", *Wind Energy Science* **7** (2), 2022. https://doi.org/10.5194/wes-7-585-2022.

[32] Splettstößer, W. R., van der Wall, B. G., Junker, B., Schultz, K.-J., Beaumier, P., Delrieux, Y., Leconte, P., Crozier, P.: "The ERATO Programme: Wind Tunnel Results and Proof of Design for an Aeroacoustically Optimized Rotor", 25th European Rotorcraft Forum, Rome, Italy, Sept 14–16, 1999.

[33] Uluocak, S., Perçin, M., Uzol, O.: "Experimental Investigation of Tip Anhedral Effects on the Aerodynamics of a Model Helicopter Rotor in Hover", *Aerospace Science and Technology*, **113**, 2021. https://doi.org/10.1016/j.ast.2021.106671.

[34] van der Wall, B. G., Richard, H.: "Analysis Methodology for 3C-PIV Data of Rotory Wing Vortices", *Experiments in Fluids* **40** (5), 2006. https://doi.org/10.1007/s00348-006-0117-x.

[35] van der Wall, B. G., Kessler, C., Delrieux, Y., Beaumier, P., Gervais, M., Hirsch, J.-F., Pengel, K., Crozier, P.: "From ERATO Basic Research to the Blue Edge^{TM} Rotor Blade", 72nd Annual Forum of the American Helicopter Society, West Palm Beach, FL, USA, May 17–19, 2016.

[36] Weiss, A., Geisler, R., Müller, M. M., Klein, C., Henne, U., Braukmann, J. N., Letzgus, J.: "Dynamic-Stall Measurements using Time-Resolved Pressure-Sensitive Paint on Double-Swept Rotor Blades", *Experiments in Fluids* **63** (15), 2022. https://doi.org/10.1007/s00348-021-03366-6.

[37] Whitehouse, G. R., Wachspress, D. A., Quackenbush, T. R.: "Predicting the Influence of Blade Shape on Hover Performance with Comprehensive Analysis", *Journal of Aircraft* **55** (1), 2018. https://doi.org/10.2514/1.C034073.

[38] Widjaja, R., Lim, J. W., Jain, R., Potsdam, M.: "Investigation of BERP-Shape Tip Design on an Apache Rotor Blade", 76th Annual Forum of the Vertical Flight Society, Virtual, Oct 6–8, 2020.

[39] Wilke, G., Bailly, J., Kimura, K., Tanabe, Y.: "JAXA-ONERA-DLR Cooperation: Results from Rotor Optimization in Hover", *CEAS Aeronautical Journal* **13**, 2022. https://doi.org/10.1007/s13272-022-00580-8.

[40] Wong, O. D., Watkins, A. N., Goodman, K. Z., Crafton, J., Forlines, A., Goss, L., Gregory, J. W., Juliano, T. J.: "Blade Tip Pressure Measurements Using Pressure-Sensitive Paint", *Journal of the American Helicopter Society*, **63** (2), 1999. https://doi.org/10.4050/JAHS.63.012001.

[41] Wolf, C. C., Braukmann, J. N., Stauber, W., Schwermer, T., Raffel, M.: "The Tip Vortex System of a Four-Bladed Rotor in Dynamic Stall Conditions", *Journal of the American Helicopter Society*, **64** (2), 2019. https://doi.org/10.4050/JAHS.64.022005.

[42] Wolf, C. C., Weiss, A., Schwarz, C., Braukmann, J. N., Koch, S., Raffel, M.: "Wake Unsteadiness and Tip Vortex System of Full-Scale Helicopters in Ground Effect", *Journal of the American Helicopter Society*, **67** (1), 2022. https://doi.org/10.4050/JAHS.67.012010.

[43] Yamauchi, G. K., Wadcock, A. J., Ramasamy, M.: "Wind Tunnel Measurements of Full-Scale UH-60A Rotor Tip Vortices", 68th Annual Forum of the American Helicopter Society, Fort Worth, TX, USA, May 1–3, 2012.